Progress In Electromagnetics Research, PIER 65, 201–232, 2006

VECTOR SPECTRAL-DOMAIN METHOD FOR THE ANALYSIS OF FREQUENCY SELECTIVE SURFACES

A. Qing

Temasek Laboratories
National University of Singapore
5 Sports Drive 2, Singapore 117508

Abstract—Standard spectral-domain method (SDM) is one of the popular approaches to analyze frequency selective surfaces (FSS). However, it is inherently incapable of handling normal incidence because of its dubious definition of excitation fields, reflection and transmission coefficients using z-component of vector potentials. Moreover, as far as the author knows, it has never been applied to analyze FSS with gangbuster arrays. In this paper, an improved SDM, the vector spectral-domain method, is presented. By proving the equivalence of the spectra of unit cell current and element current, the scattered field from FSS structures is formulated in terms of spectral-domain element current instead of spectral-domain unit cell current. Galerkin's method is applied to obtain the unknown induced surface current. Well-established definition of excitation fields, reflection and transmission coefficients is adopted. Extensive experimental validation has been conducted.

1. INTRODUCTION

1.1. Geometry of Frequency Selective Surfaces

Frequency selective surfaces (FSS) [1–4] have been widely applied in various engineering areas. An FSS contains one or more periodic arrays (red lines in Fig. 1) embedded in multilayered dielectric structure. Without loss of generality, the array elements are assumed to be perfect electric conductors (PEC). It is further assumed that array elements are one-dimensional thin wires and/or two-dimensional patches unless specified otherwise. Several typical array patterns are shown in Fig. 2.

An array is generated by repeating its reference element (element 00) along two non-trivial directions $\hat{s}_a$ with periodicity T_a and $\hat{s}_b$ with

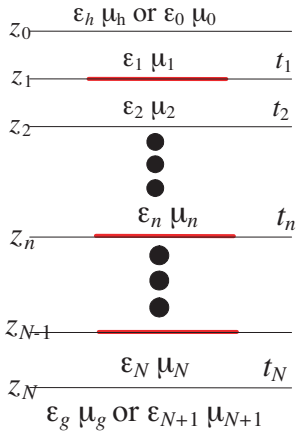

Figure 1. Cross section of an FSS structure.

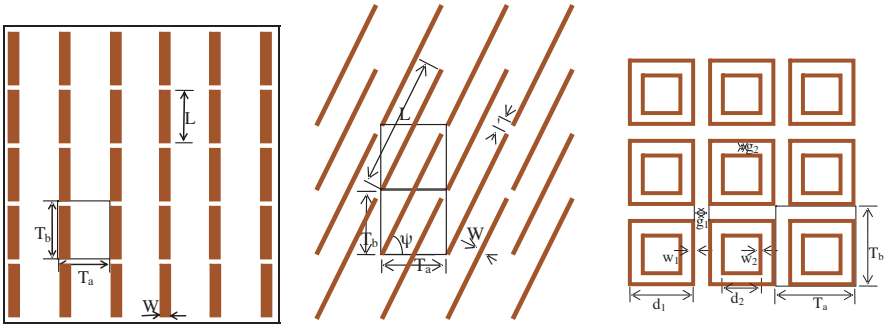

(a) thin dipole (b) type-2 gangbuster (c) double square

Figure 2. Typical array patterns.

periodicity T_b. Ω^e_{mn} is the domain in which element (m, n) is embedded. Alternatively, the array is generated by repeating its reference unit cell (unit cell 00) in the same way as described above. A unit cell is a parallelogram with side vectors $\boldsymbol{S}_a = \hat{s}_a T_a$ and $\boldsymbol{S}_b = \hat{s}_b T_b$. Ω^u_{mn} is the domain unit cell (m, n) occupies. The reference element and the reference unit cell for a type-2 gangbuster array is shown in Fig. 3.

Generally speaking, $\Omega^e_{mn} \neq \Omega^u_{mn}$. In addition, we have

$$\Omega^u_{mn} \cap \Omega^u_{m'n'} = \delta_{mm'}\delta_{nn'}\Omega^u_{mn}, \tag{1}$$

where δ_{mn} is the Kronecker symbol.

The relationship specified in (1) means that unit cells do not

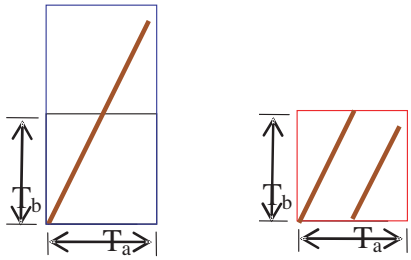

(a) Reference Element (b) Reference Unit Cell

Figure 3. Reference element and reference unit cell of a Type-2 gangbuster array.

overlap with each other. However, there may be no similar relationship for Ω^e_{mn} and $\Omega^e_{m'n'}$.

Arrays in an FSS structure are not necessarily identical. In addition, different arrays may have different periodicity. Usually, periodicities of different arrays satisfy

$$m\boldsymbol{S}_a^{l_1} = n\boldsymbol{S}_a^{l_2} \qquad p\boldsymbol{S}_b^{l_1} = q\boldsymbol{S}_b^{l_2}, \tag{2}$$

where m and n do not have common divisors. The same is true for p and q. $1 \le l_1,\ l_2 \le L,\ L$ is the total number of arrays.

For simplicity, here, we assume

$$\boldsymbol{S}_a^{l_1} = \boldsymbol{S}_a^{l_2} \qquad \boldsymbol{S}_b^{l_1} = \boldsymbol{S}_b^{l_2}, \tag{3}$$

1.2. Incident Field

Throughout this paper, FSS structures are assumed to be illuminated by plane wave (time factor $e^{j\omega t}$ is assumed and suppressed)

$$\boldsymbol{E}^{inc}(\boldsymbol{r}) = \boldsymbol{E}_0^{inc} e^{-j\boldsymbol{k}^{inc}\cdot\boldsymbol{r}}, \tag{4}$$

where $\boldsymbol{E}_0^{inc} = \boldsymbol{E}_{0\|}^{inc} + \boldsymbol{E}_{0\perp}^{inc}$ is the amplitude of incident field, $\boldsymbol{E}_{0\|}^{inc}$ ($\|\hat{\theta}^{inc}$) and $\boldsymbol{E}_{0\perp}^{inc}$ ($\|\hat{\phi}^{inc}$) are the parallel and perpendicular components with respect to the plane of incidence as shown in Fig. 4. $\boldsymbol{k}^{inc} = \boldsymbol{k}_\rho^{inc} - \hat{z}k_z^{inc}$ is the propagation vector. $\boldsymbol{k}_\rho^{inc} = -k_\rho^{inc}\widetilde{\hat{\rho}}^{inc}$, $k_z^{inc} = k_h\cos\theta^{inc}$. $k_\rho^{inc} = k_h\sin\theta^{inc}$, $\widetilde{\hat{\rho}}^{inc} = \cos\phi^{inc}\hat{x} + \sin\phi^{inc}\hat{y}$. k_h is the wave number in the host medium, $k_h^2 = \omega^2\mu_h\varepsilon_h$, ω is the angular frequency, μ_h and ε_h are the permeability and permittivity of the host medium, θ^{inc} and ϕ^{inc} are the elevation and azimuthal incident angles, respectively.

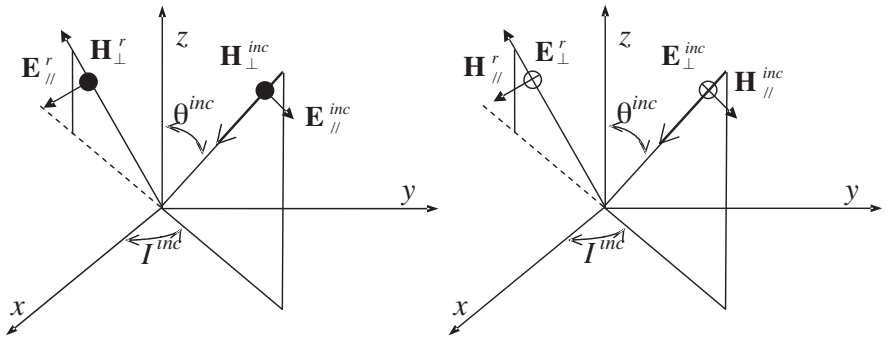

Figure 4. Plane of incidence and polarization of incident field (left: parallel polarization, right: perpendicular polarization).

1.3. Analysis of Frequency Selective Surfaces

Analysis of FSS structures is of great interest to both design and application engineers. Many approaches such as the periodic moment method [4], the standard spectral-domain method (SDM) [5, 6], the equivalent circuit model [7], the finite element method [8], the finite difference time domain method [9, 10], the recursive T-matrix method [11, 12], etc., have been proposed.

Among various methods for the analysis of FSS, the standard SDM is usually the method of choice.

1.4. Applications of Frequency Selective Surfaces

As mentioned before, FSS have been widely applied in various engineering areas [1–4]. Recently, FSS found its applications in metamaterials [13–16].

1.5. Fourier Transform

For the convenience of the following description, let's define the Fourier transform first.

$$\begin{aligned} \widetilde{f}(\boldsymbol{k}_\rho, z) &= \int_{-\infty}^{\infty}\int_{-\infty}^{\infty} f(\boldsymbol{r}) e^{j\boldsymbol{k}_\rho\cdot\boldsymbol{\rho}} d\boldsymbol{\rho} \\ f(\boldsymbol{r}) &= \frac{1}{(2\pi)^2}\int_{-\infty}^{\infty}\int_{-\infty}^{\infty} \widetilde{f}(\boldsymbol{k}_\rho, z) e^{-j\boldsymbol{k}_\rho\cdot\boldsymbol{\rho}} d\boldsymbol{k}_\rho \end{aligned}, \tag{5}$$

where $\boldsymbol{r} = \boldsymbol{\rho} + z\hat{z},\ \boldsymbol{\rho} = x\hat{x} + y\hat{y},\ \boldsymbol{k}_\rho = k_\rho\widetilde{\hat{\rho}} = \alpha\hat{x} + \beta\hat{y}$.

2. STANDARD SPECTRAL-DOMAIN METHOD

2.1. Scattered Field from an Freestanding FSS

The standard SDM first uses Fourier transform to formulate the tangential components of spatial-domain scattered field from scatterers in the reference unit cell Ω_{00}^u, $E_x^{su}(\boldsymbol{r})$ and $E_y^{su}(\boldsymbol{r})$, as the Fourier integral of the tangential spectral-domain scattered field, $\widetilde{E}_x^{su}(\boldsymbol{k}_\rho, z)$ and $\widetilde{E}_y^{su}(\boldsymbol{k}_\rho, z)$,

$$\left[\begin{array}{c} E_x^{su}(\boldsymbol{r}) \\ E_y^{su}(\boldsymbol{r}) \end{array}\right] = \frac{1}{(2\pi)^2} \int_{-\infty}^{\infty}\int_{-\infty}^{\infty} \left[\begin{array}{c} \widetilde{E}_x^{su}(\boldsymbol{k}_\rho, z) \\ \widetilde{E}_y^{su}(\boldsymbol{k}_\rho, z) \end{array}\right] e^{-j\boldsymbol{k}_\rho\cdot\boldsymbol{\rho}} d\boldsymbol{k}_\rho, \tag{6}$$

where

$$\left[\begin{array}{c} \widetilde{E}_x^{su}(\boldsymbol{k}_\rho, z) \\ \widetilde{E}_y^{su}(\boldsymbol{k}_\rho, z) \end{array}\right] = \left\{ \overline{\overline{\boldsymbol{G}}}_h^{\rho}(\boldsymbol{k}_\rho, z, z') \left[\begin{array}{c} \widetilde{J}_x^u(\boldsymbol{k}_\rho, z') \\ \widetilde{J}_y^u(\boldsymbol{k}_\rho, z') \end{array}\right] \right\}_{z'=0}, \tag{7}$$

$\widetilde{\boldsymbol{J}}^u(\boldsymbol{k}_\rho, z) = \hat{x}\widetilde{J}_x^u(\boldsymbol{k}_\rho, z) + \hat{y}\widetilde{J}_y^u(\boldsymbol{k}_\rho, z)$ is the induced spectral-domain surface unit cell current whose spatial-domain counterpart is $\boldsymbol{J}^u(\boldsymbol{r}) = \hat{x}J_x^u(\boldsymbol{r}) + \hat{y}J_y^u(\boldsymbol{r})$,

$$\begin{aligned} \overline{\overline{\boldsymbol{G}}}_h^{\rho}(\boldsymbol{k}_\rho, z, z') &= \frac{1}{j\omega\varepsilon_h} \left[\begin{array}{cc} k_h^2-\alpha^2 & -\alpha\beta \\ -\alpha\beta & k_h^2-\beta^2 \end{array}\right] \widetilde{G}_h(\boldsymbol{k}_\rho, z, z') \\ &= \left[\begin{array}{cc} \overline{\overline{G}}_h^{xx} & \overline{\overline{G}}_h^{xy} \\ \overline{\overline{G}}_h^{yx} & \overline{\overline{G}}_h^{yy} \end{array}\right], \end{aligned} \tag{8}$$

$$\widetilde{G}_h(\boldsymbol{k}_\rho, z, z') = \frac{e^{-jk_z|z-z'|}}{2jk_z} \tag{9}$$

is the scalar spectral-domain Greens' functions, $k_z = \sqrt{k_h^2 - k_\rho^2} = k_z' - jk_z''$ with $k_z'' \geq 0$.

By using Floquet's theorem, the tangential components of scattered field from the FSS, $E_x^{sa}(\boldsymbol{r})$ and $E_y^{sa}(\boldsymbol{r})$, is obtained by converting the Fourier integral in (6) into summation of Floquet modes,

$$\left[\begin{array}{c} E_x^{sa}(\boldsymbol{r}) \\ E_y^{sa}(\boldsymbol{r}) \end{array}\right] = \frac{1}{T_a T_b} \sum_{p=-\infty}^{\infty}\sum_{q=-\infty}^{\infty} \left[\begin{array}{c} \widetilde{E}_x^{sa}\left(\boldsymbol{k}_\rho^{pq}, z\right) \\ \widetilde{E}_y^{sa}\left(\boldsymbol{k}_\rho^{pq}, z\right) \end{array}\right] e^{-j\boldsymbol{k}_\rho^{pq}\cdot\boldsymbol{\rho}}, \tag{10}$$

where $\boldsymbol{k}_\rho^{pq} = k_\rho^{pq}\widetilde{\hat{\rho}}_{pq} = p\widetilde{\boldsymbol{S}}_a + q\widetilde{\boldsymbol{S}}_b + \boldsymbol{k}_\rho^{inc} = \alpha_{pq}\hat{x} + \beta_{pq}\hat{y}$, $\widetilde{\boldsymbol{S}}_a$ and $\widetilde{\boldsymbol{S}}_b$ are the spectral-domain base vectors of a spectral-domain unit cell (reciprocal unit cell) [17].

2.2. Galerkin's Implementation

Expand the surface unit cell current as

$$\boldsymbol{J}^u(\boldsymbol{r}) = \hat{x}\sum_{i=1}^{M} I_{xi}^u B_{xi}^u(\boldsymbol{r}) + \hat{y}\sum_{j=1}^{N} I_{yj}^u B_{yj}^u(\boldsymbol{r}) \quad \boldsymbol{r} \in \Omega_{00}^u, \tag{11}$$

where $B_{xi}^u(\boldsymbol{r})$ and $B_{yj}^u(\boldsymbol{r})$ are the spatial-domain unit cell current basis functions, I_{xi}^u and I_{yj}^u are the corresponding unknown expansion coefficient.

Implementing Galerkin's method over (10) with the boundary condition that the tangential electric field on the surface of conducting scatterers vanishes, we obtain the following matrix equation

$$\left[\begin{array}{c} \boldsymbol{V}_x \\ \boldsymbol{V}_y \end{array}\right] = \left[\begin{array}{cc} \boldsymbol{Z}_{xx} & \boldsymbol{Z}_{xy} \\ \boldsymbol{Z}_{yx} & \boldsymbol{Z}_{yy} \end{array}\right] \cdot \left[\begin{array}{c} \boldsymbol{I}_x \\ \boldsymbol{I}_y \end{array}\right] \tag{12}$$

where

$$V_{ai} = -E_{0a}^{inc} \int\limits_{\Omega_{00}^u} B_{ai}^u(\boldsymbol{r}) e^{-j\boldsymbol{k}^{inc}\cdot\boldsymbol{r}} d\boldsymbol{\rho} = -E_{0a}^{inc} \widetilde{B}_{ai}^u\left(-\boldsymbol{k}_\rho^{inc}, 0\right)$$

$$[\boldsymbol{Z}_{ab}]_{ij} = \frac{1}{T_a T_b} \int\limits_{\Omega_{00}^u} B_{ai}^u(\boldsymbol{r}) \sum_{p=-\infty}^{\infty}\sum_{q=-\infty}^{\infty} \overline{\overline{\widetilde{G}}}_h^{ab}\left(\boldsymbol{k}_\rho^{pq},0,0\right) \widetilde{B}_{bj}^u\left(\boldsymbol{k}_\rho^{pq},0\right) e^{-j\boldsymbol{\rho}\cdot\boldsymbol{k}_\rho^{pq}} d\boldsymbol{\rho}$$

$$= \frac{1}{T_a T_b} \sum_{p=-\infty}^{\infty}\sum_{q=-\infty}^{\infty} \widetilde{B}_{ai}^u\left(-\boldsymbol{k}_\rho^{pq}, 0\right) \overline{\overline{\widetilde{G}}}_h^{ab}\left(\boldsymbol{k}_\rho^{pq}, 0, 0\right) \widetilde{B}_{yj}^u\left(\boldsymbol{k}_\rho^{pq}, 0\right)$$

2.3. Excitation Field

The excitation (incident) electric field is formulated as

$$\boldsymbol{E}_{TM}^{inc}(\boldsymbol{r}) = \frac{1}{j\omega\varepsilon_h} \nabla\times\nabla\times\boldsymbol{A}^{inc}(\boldsymbol{r}) = \frac{1}{j\omega\varepsilon_h} \nabla\times\nabla\times\left(\hat{z}e^{-j\boldsymbol{k}^{inc}\cdot\boldsymbol{r}}\right), \tag{13}$$

$$\boldsymbol{E}_{TE}^{inc}(\boldsymbol{r}) = -\nabla\times\boldsymbol{F}^{inc}(\boldsymbol{r}) = -\nabla\times\left(\hat{z}e^{-j\boldsymbol{k}^{inc}\cdot\boldsymbol{r}}\right), \tag{14}$$

$\boldsymbol{E}_0^{inc} = \hat{x}E_{0x}^{inc} + \hat{y}E_{0y}^{inc}$ can be obtained accordingly.

2.4. Reflection and Transmission Coefficients

The reflection and transmission coefficients are defined as

$$\boldsymbol{A}^r(\boldsymbol{r}) = \hat{z}\sum_{p=-\infty}^{\infty}\sum_{q=-\infty}^{\infty} R_{pq}^{TM} e^{-j\boldsymbol{k}_{pq}^r\cdot\boldsymbol{r}}, \tag{15}$$

$$\boldsymbol{F}^r(\boldsymbol{r}) = \hat{z} \sum_{p=-\infty}^{\infty} \sum_{q=-\infty}^{\infty} R_{pq}^{TE} e^{-j\boldsymbol{k}_{pq}^r \cdot \boldsymbol{r}}, \tag{16}$$

$$\boldsymbol{A}^t(\boldsymbol{r}) = \hat{z} \sum_{p=-\infty}^{\infty} \sum_{q=-\infty}^{\infty} T_{pq}^{TM} e^{-j\boldsymbol{k}_{pq}^t \cdot \boldsymbol{r}}, \tag{17}$$

$$\boldsymbol{F}^t(\boldsymbol{r}) = \hat{z} \sum_{p=-\infty}^{\infty} \sum_{q=-\infty}^{\infty} T_{pq}^{TE} e^{-j\boldsymbol{k}_{pq}^t \cdot \boldsymbol{r}}, \tag{18}$$

where the superscripts r and t stand for reflection and transmission respectively, $\boldsymbol{k}_{pq}^r = \boldsymbol{k}_\rho^{pq} + \hat{z}k_{zpq}^h$, $\boldsymbol{k}_{pq}^t = \boldsymbol{k}_\rho^{pq} - \hat{z}k_{zpq}^g$, the superscripts h and g stands for host medium and ground medium respectively, $k_{zpq}^h = \sqrt{k_h^2 - (k_\rho^{pq})^2}$, $k_{zpq}^g = \sqrt{k_g^2 - (k_\rho^{pq})^2}$, k_g is the wave number in the ground medium, $k_g^2 = \omega^2 \mu_g \varepsilon_g$, μ_g and ε_g are the permeability and permittivity of the ground medium.

After tedious manipulations, the reflection and transmission coefficients are obtained as

$$R_{pq}^{TE} = \left. \frac{\begin{pmatrix} \beta_{pq}\left[\widetilde{E}_x^{sa}\left(\boldsymbol{k}_\rho^{pq}, z\right) + \delta_{p0}\delta_{q0}\widetilde{E}_{0x}^r\left(\boldsymbol{k}_\rho^{00}, z\right)\right] \\ -\alpha_{pq}\left[\widetilde{E}_y^{sa}\left(\boldsymbol{k}_\rho^{pq}, z\right) + \delta_{p0}\delta_{q0}\widetilde{E}_{0y}^r\left(\boldsymbol{k}_\rho^{00}, z\right)\right] \end{pmatrix}}{j\left(k_\rho^{pq}\right)^2} \right|_{z=0}, \tag{19}$$

$$R_{pq}^{TM} = \left. \frac{\begin{pmatrix} \alpha_{pq}\left[\widetilde{E}_x^{sa}\left(\boldsymbol{k}_\rho^{pq}, z\right) + \delta_{p0}\delta_{q0}\widetilde{E}_{0x}^r\left(\boldsymbol{k}_\rho^{00}, z\right)\right] \\ +\beta_{pq}\left[\widetilde{E}_y^{sa}\left(\boldsymbol{k}_\rho^{pq}, z\right) + \delta_{p0}\delta_{q0}\widetilde{E}_{0y}^r\left(\boldsymbol{k}_\rho^{00}, z\right)\right] \end{pmatrix}}{j\left(k_\rho^{pq}\right)^2 k_{zpq}^h/\omega\varepsilon_h} \right|_{z=0}, \tag{20}$$

$$T_{pq}^{TE} = \left. \frac{\begin{pmatrix} \beta_{pq}\left[\widetilde{E}_x^{sa}\left(\boldsymbol{k}_\rho^{pq}, z\right) + \delta_{p0}\delta_{q0}\widetilde{E}_{0x}^t\left(\boldsymbol{k}_\rho^{00}, z\right)\right] \\ -\alpha_{pq}\left[\widetilde{E}_y^{sa}\left(\boldsymbol{k}_\rho^{pq}, z\right) + \delta_{p0}\delta_{q0}\widetilde{E}_{0y}^t\left(\boldsymbol{k}_\rho^{00}, z\right)\right] \end{pmatrix}}{j\left(k_\rho^{pq}\right)^2} \right|_{z=z_N}, \tag{21}$$

$$T_{pq}^{TM} = \left. \frac{\begin{pmatrix} \alpha_{pq}\left[\widetilde{E}_x^{sa}\left(\boldsymbol{k}_\rho^{pq}, z\right) + \delta_{p0}\delta_{q0}\widetilde{E}_{0x}^t\left(\boldsymbol{k}_\rho^{00}, z\right)\right] \\ +\beta_{pq}\left[\widetilde{E}_y^{sa}\left(\boldsymbol{k}_\rho^{pq}, z\right) + \delta_{p0}\delta_{q0}\widetilde{E}_{0y}^t\left(\boldsymbol{k}_\rho^{00}, z\right)\right] \end{pmatrix}}{-jk_{zpq}^g\left(k_\rho^{pq}\right)^2/\omega\varepsilon_g} \right|_{z=z_N}, \tag{22}$$

where $\widetilde{E}_{0x}^{r/t}(\boldsymbol{k}_\rho^{00}, z)$ and $\widetilde{E}_{0y}^{r/t}(\boldsymbol{k}_\rho^{00}, z)$ are the tangential components of the spectral-domain reflected or transmitted field from the multilayered dielectric structure without arrays embedded.

2.5. Disadvantages

Although standard SDM is usually the method of choice for the analysis of FSS structures, it is found to have the following disadvantages

(a) The standard SDM is unable to handle normal incidence although performance of FSS structures at normal incidence is often the first priority. To the best knowledge of this author, the usage of z-directed vector potentials is the prime culprit,
(1) The tangential incident electric field (excitation field) expressed in (13) and (14) vanishes at normal incidence.
(2) The reflection and transmission coefficients of the FSS structure at normal incidence expressed in (19)–(22) are indefinite.
People applying standard SDM usually replace normal incidence by a very small incident elevation angle and/or a very small azimuthal angle [1, 5, 18–21]. Although engineering acceptable approximate results can be obtained by this practice, it is not a serious and scientific way to solve problems.

(b) The transmission and reflection coefficients are confusing. Their amplitude can even be larger than 1. Worst of all, they are not experimentally observable quantities.

(c) The scattered field is formulated in terms of spectral-domain unit cell current as shown in (7). Researchers may take it for granted that an element must be confined by a unit cell. However, in FSS structures with gangbuster arrays, an array element cannot be confined by a unit cell. As far as this author knows, there is no public literature about analyzing FSS structures with gangbuster arrays using standard SDM.

2.6. Solutions

On account of the aforementioned disadvantages of standard SDM, in this paper, an improved SDM, the vector spectral-domain method (VSM), is developed. It follows the basic idea of standard SDM. The spectral-domain element current and the spectral-domain unit cell current have been proven equal. Therefore, scattered field from FSS structures is formulated in terms of spectral-domain element current. Well-established definitions of excitation fields, reflection and transmission coefficients are applied.

3. VECTOR SPECTRAL-DOMAIN METHOD

3.1. Scattered Field from FSS Structures

3.1.1. Scattered Field from Scatterers in the Reference Unit Cell of a Freestanding FSS

The scattered electric field from scatterers in the reference unit cell is

$$\boldsymbol{E}^{su}(\boldsymbol{r}) = \frac{1}{j\omega\varepsilon_h}\nabla\times\nabla\times\boldsymbol{A}^u(\boldsymbol{r}), \tag{23}$$

where

$$\boldsymbol{A}^u(\boldsymbol{r}) = \iint\limits_{\Omega^u_{00}} G_h(\boldsymbol{r},\boldsymbol{r}')\boldsymbol{J}^u(\boldsymbol{r}')d\boldsymbol{r}'$$
$$G_h(\boldsymbol{r},\boldsymbol{r}') = \frac{e^{-jk_h|\boldsymbol{r}-\boldsymbol{r}'|}}{4\pi|\boldsymbol{r}-\boldsymbol{r}'|}$$

(23) is rewritten as

$$\begin{aligned}\boldsymbol{E}^{su}(\boldsymbol{r}) &= \frac{1}{j\omega\varepsilon_h}\nabla\times\nabla\times\frac{1}{(2\pi)^2}\int\limits_{-\infty}^{\infty}\int\limits_{-\infty}^{\infty}\left\{\widetilde{G}_h(\boldsymbol{k}_\rho,z,z')\widetilde{\boldsymbol{J}}^u(\boldsymbol{k}_\rho,z')\right\}_{z'=0}\\ &\quad\times e^{-j\boldsymbol{\rho}\cdot\boldsymbol{k}_\rho}d\boldsymbol{k}_\rho,\end{aligned} \tag{24}$$

Substituting (9) into (24), we have

$$\begin{aligned}\boldsymbol{E}^{su}(\boldsymbol{r}) &= \frac{1}{j\omega\varepsilon_h}\nabla\times\nabla\times\frac{1}{(2\pi)^2}\int\limits_{-\infty}^{\infty}\int\limits_{-\infty}^{\infty}\left\{\frac{e^{-jk_z|z-z'|}}{2jk_z}\widetilde{\boldsymbol{J}}^u\left(\boldsymbol{k}_\rho,z'\right)\right\}_{z'=0}\\ &\quad\times e^{-j\boldsymbol{\rho}\cdot\boldsymbol{k}_\rho}d\boldsymbol{k}_\rho\\ &= \frac{1}{(2\pi)^2}\int\limits_{-\infty}^{\infty}\int\limits_{-\infty}^{\infty}\left\{\frac{-1}{\omega\varepsilon_h}\frac{e^{\pm jk_zz'}}{2k_z}\nabla\times\nabla\times\left[e^{-j\boldsymbol{k}^s\cdot\boldsymbol{r}}\widetilde{\boldsymbol{J}}^u(\boldsymbol{k}_\rho,z')\right]\right\}_{z'=0}d\boldsymbol{k}_\rho\end{aligned} \tag{25}$$

where $\boldsymbol{k}^s = \boldsymbol{k}_\rho \pm k_z\hat{z}$ is the propagation vector of the plane wave spectrum of the scattered field , the plus and minus signs apply to cases $z > z'$ and $z \le z'$ respectively.

Completing the curl operations in (25), we have

$$\begin{aligned}\boldsymbol{E}^{su}(\boldsymbol{r}) &= \frac{1}{(2\pi)^2}\int\limits_{-\infty}^{\infty}\int\limits_{-\infty}^{\infty}\left\{\frac{1}{\omega\varepsilon_h}\frac{e^{-jk_z|z-z'|}}{2k_z}\boldsymbol{k}^s\times\boldsymbol{k}^s\times\widetilde{\boldsymbol{J}}^u\left(\boldsymbol{k}_\rho,z'\right)\right\}_{z'=0}\\ &\quad\times e^{-j\boldsymbol{\rho}\cdot\boldsymbol{k}_\rho}d\boldsymbol{k}_\rho,\end{aligned} \tag{26}$$

Therefore,

$$\boldsymbol{E}^{su}(\boldsymbol{r}) = \frac{1}{(2\pi)^2} \int\limits_{-\infty}^{\infty} \int\limits_{-\infty}^{\infty} \widetilde{\boldsymbol{E}}^{su}(\boldsymbol{k}_\rho, z) e^{-j\boldsymbol{\rho}\cdot\boldsymbol{k}_\rho} d\boldsymbol{k}_\rho, \tag{27}$$

where

$$\begin{aligned} \widetilde{\boldsymbol{E}}^{su}(\boldsymbol{k}_\rho, z) &= \left\{ \frac{1}{\omega\varepsilon_h} \frac{e^{-jk_z|z-z'|}}{2k_z} \boldsymbol{k}^s \times \boldsymbol{k}^s \times \widetilde{\boldsymbol{J}}^u(\boldsymbol{k}_\rho, z') \right\}_{z'=0} \\ &= \left\{ \overline{\overline{\widetilde{\boldsymbol{G}}}}_h(\boldsymbol{k}_\rho, z, z') \cdot \widetilde{\boldsymbol{J}}^u(\boldsymbol{k}_\rho, z') \right\}_{z'=0} \end{aligned}$$

3.1.2. Spectrum of Unit Cell Current

In order to find the spectrum of the unit cell current, define

$$\boldsymbol{J}'(\boldsymbol{r}) = \boldsymbol{J}^u(\boldsymbol{r}) e^{j\boldsymbol{k}_\rho^{inc}\cdot\boldsymbol{\rho}}, \tag{28}$$

Accordingly,

$$\widetilde{\boldsymbol{J}}'(\boldsymbol{k}_\rho, z) = \widetilde{\boldsymbol{J}}^u\left(\boldsymbol{k}_\rho + \boldsymbol{k}_\rho^{inc}, z\right), \tag{29}$$

According to the Floquet's theorem, we have

$$\boldsymbol{J}^u(\boldsymbol{r} + m\boldsymbol{S}_a + n\boldsymbol{S}_b) = \boldsymbol{J}^u(\boldsymbol{r}) e^{-j\boldsymbol{k}_\rho^{inc}\cdot(m\boldsymbol{S}_a + n\boldsymbol{S}_b)}, \tag{30}$$

It is very easy to prove that

$$\boldsymbol{J}'(\boldsymbol{r} + m\boldsymbol{S}_a + n\boldsymbol{S}_b) = \boldsymbol{J}^u(\boldsymbol{r} + m\boldsymbol{S}_a + n\boldsymbol{S}_b) e^{j\boldsymbol{k}_\rho^{inc}\cdot(\boldsymbol{\rho} + m\boldsymbol{S}_a + n\boldsymbol{S}_b)} = \boldsymbol{J}'(\boldsymbol{r}), \tag{31}$$

Therefore,

$$\boldsymbol{J}'(\boldsymbol{r}) = \frac{1}{T_a T_b} \sum_{p=-\infty}^{\infty} \sum_{q=-\infty}^{\infty} \widetilde{\boldsymbol{J}}'\left(p\widetilde{\boldsymbol{S}}_a + q\widetilde{\boldsymbol{S}}_b, z\right) e^{-j\boldsymbol{\rho}\cdot(p\widetilde{\boldsymbol{S}}_a + q\widetilde{\boldsymbol{S}}_b)}, \tag{32}$$

$$\widetilde{\boldsymbol{J}}'\left(p\widetilde{\boldsymbol{S}}_a + q\widetilde{\boldsymbol{S}}_b, z\right) = \iint\limits_{\Omega_{00}^u} \boldsymbol{J}'(\boldsymbol{r}) e^{j\boldsymbol{\rho}\cdot(p\widetilde{\boldsymbol{S}}_a + q\widetilde{\boldsymbol{S}}_b)} d\boldsymbol{\rho}, \tag{33}$$

The integration domain in (33) is specified as Ω_{00}^u, the domain of unit cell $(0, 0)$. However, we have

$$\boldsymbol{S}_i \cdot \widetilde{\boldsymbol{S}}_j = 2\pi\delta_{ij}, \tag{34}$$

Therefore, the integration domain can be the domain of arbitrary unit cell.

Using (28) into (32), we have

$$\begin{aligned}\boldsymbol{J}^u(\boldsymbol{r}) &= \boldsymbol{J}'(\boldsymbol{r})e^{-j\boldsymbol{k}_\rho^{inc}\cdot\boldsymbol{\rho}} \\ &= \frac{1}{T_aT_b}\sum_{p=-\infty}^{\infty}\sum_{q=-\infty}^{\infty}\widetilde{\boldsymbol{J}}'\Big(p\widetilde{\boldsymbol{S}}_a+q\widetilde{\boldsymbol{S}}_b,z\Big)e^{-j\boldsymbol{\rho}\cdot(p\widetilde{\boldsymbol{S}}_a+q\widetilde{\boldsymbol{S}}_b)}e^{-j\boldsymbol{k}_\rho^{inc}\cdot\boldsymbol{\rho}}, \quad (35)\end{aligned}$$

Using (28), (29) and (33), we have

$$\begin{aligned}\widetilde{\boldsymbol{J}}^u\left(\boldsymbol{k}_\rho^{pq},z\right) &= \widetilde{\boldsymbol{J}}'\left(p\widetilde{\boldsymbol{S}}_a+q\widetilde{\boldsymbol{S}}_b,z\right) = \iint\limits_{\Omega_{00}^u}\boldsymbol{J}'(\boldsymbol{r})e^{j\boldsymbol{\rho}\cdot(p\widetilde{\boldsymbol{S}}_a+q\widetilde{\boldsymbol{S}}_b)}d\boldsymbol{\rho} \\ &= \iint\limits_{\Omega_{00}^u}\boldsymbol{J}^u(\boldsymbol{r})e^{-j\boldsymbol{k}_\rho^{inc}\cdot\boldsymbol{\rho}}e^{j\boldsymbol{\rho}\cdot(p\widetilde{\boldsymbol{S}}_a+q\widetilde{\boldsymbol{S}}_b)}d\boldsymbol{\rho} \\ &= \iint\limits_{\Omega_{00}^u}\boldsymbol{J}^u(\boldsymbol{r})e^{-j\boldsymbol{\rho}\cdot\boldsymbol{k}_\rho^{pq}}d\boldsymbol{\rho}, \quad (36)\end{aligned}$$

Therefore,

$$\boldsymbol{J}^u(\boldsymbol{r}) = \frac{1}{T_aT_b}\sum_{p=-\infty}^{\infty}\sum_{q=-\infty}^{\infty}\widetilde{\boldsymbol{J}}^u\left(\boldsymbol{k}_\rho^{pq},z\right)e^{-j\boldsymbol{\rho}\cdot\boldsymbol{k}_\rho^{pq}}, \quad (37)$$

3.1.3. Scattered Field from an Freestanding FSS in Terms of Spectral-domain Unit Cell Current

Apparently, the scattered field from the freestanding FSS is

$$\boldsymbol{E}^{sa}(\boldsymbol{r}) = \frac{1}{T_aT_b}\sum_{p=-\infty}^{\infty}\sum_{q=-\infty}^{\infty}\widetilde{\boldsymbol{E}}^{sa}\left(\boldsymbol{k}_\rho^{pq},z\right)e^{-j\boldsymbol{\rho}\cdot\boldsymbol{k}_\rho^{pq}}, \quad (38)$$

where

$$\widetilde{\boldsymbol{E}}^{sa}\left(\boldsymbol{k}_\rho^{pq},z\right) = \left[\overline{\overline{\widetilde{\boldsymbol{G}}}}_h\left(\boldsymbol{k}_\rho^{pq},z,z'\right)\cdot\widetilde{\boldsymbol{J}}^u\left(\boldsymbol{k}_\rho^{pq},z'\right)\right]_{z'=0}, \quad (39)$$

The formulation by far is based on the concept of unit cell current. Researchers may take it for granted that an element must be confined by a unit cell. However, in FSS structures with gangbuster arrays, an array element cannot be confined by a unit cell. To the best knowledge of this author, there is no public literature about analyzing FSS structures with gangbuster arrays using standard SDM.

3.1.4. Spectrum of Element Current

Element current $\boldsymbol{J}^e_{mn}(\boldsymbol{r} \in \Omega^e_{mn})$ and unit cell current $\boldsymbol{J}^u_{mn}(\boldsymbol{r} \in \Omega^u_{mn})$ satisfy the following relations

$$\boldsymbol{J}^u_{mn}(\boldsymbol{r}) = \sum_{m'} \sum_{n'} \boldsymbol{J}^e_{m'n'}(\boldsymbol{r}) \quad \boldsymbol{r} \in \Omega^u_{mn}, \tag{40}$$

Substituting (40) into (36), we have

$$\begin{aligned} \widetilde{\boldsymbol{J}}^u\left(\boldsymbol{k}^{pq}_\rho, z\right) &= \iint\limits_{\Omega^u_{00}} \sum_{m'} \sum_{n'} \boldsymbol{J}^e_{m'n'}(\boldsymbol{r}) e^{j\boldsymbol{\rho}\cdot\boldsymbol{k}^{pq}_\rho} d\boldsymbol{\rho} \\ &= \sum_{m'} \sum_{n'} \iint\limits_{\Omega^u_{00}\cap\Omega^e_{m'n'}} \boldsymbol{J}^e_{m'n'}(\boldsymbol{r}) e^{j\boldsymbol{\rho}\cdot\boldsymbol{k}^{pq}_\rho} d\boldsymbol{\rho}, \end{aligned} \tag{41}$$

Letting

$$\boldsymbol{\rho}\,(\in \Omega^u_{00} \cap \Omega^e_{m'n'}) = \boldsymbol{\rho}'\,(\in \Omega^e_{00} \cap \Omega^u_{-m'-n'}) + m'\boldsymbol{S}_a + n'\boldsymbol{S}_b, \tag{42}$$

$$\boldsymbol{r}\,(\in \Omega^u_{00} \cap \Omega^e_{m'n'}) = \boldsymbol{r}'\,(\in \Omega^e_{00} \cap \Omega^u_{-m'-n'}) + m'\boldsymbol{S}_a + n'\boldsymbol{S}_b, \tag{43}$$

and applying the Floquet's theorem

$$\boldsymbol{J}^e_{m'n'}(\boldsymbol{r}) = \boldsymbol{J}^e_{00}(\boldsymbol{r}') e^{-j\boldsymbol{k}^{inc}_\rho\cdot(m'\boldsymbol{S}_a + n'\boldsymbol{S}_b)} \tag{44}$$

we have

$$\begin{aligned} \widetilde{\boldsymbol{J}}^u\left(\boldsymbol{k}^{pq}_\rho, z\right) &= \sum_{m'} \sum_{n'} \iint\limits_{\Omega^e_{00}\cap\Omega^u_{-m'-n'}} \boldsymbol{J}^e_{00}(\boldsymbol{r}') e^{-j\boldsymbol{k}^{inc}_\rho\cdot(m'\boldsymbol{S}_a + n'\boldsymbol{S}_b)} \\ &\quad \times e^{j(\boldsymbol{\rho}' + m'\boldsymbol{S}_a + n'\boldsymbol{S}_b)\cdot\boldsymbol{k}^{pq}_\rho} d\boldsymbol{\rho}' \\ &= \sum_{m'} \sum_{n'} \iint\limits_{\Omega^e_{00}\cap\Omega^u_{-m'-n'}} \boldsymbol{J}^e_{00}(\boldsymbol{r}') e^{j\boldsymbol{\rho}'\cdot\boldsymbol{k}^{pq}_\rho} e^{-j\boldsymbol{k}^{inc}_\rho\cdot(m'\boldsymbol{S}_a + n'\boldsymbol{S}_b)} \\ &\quad \times e^{j(m'\boldsymbol{S}_a + n'\boldsymbol{S}_b)\cdot\boldsymbol{k}^{pq}_\rho} d\boldsymbol{\rho}' \\ &= \sum_{m'} \sum_{n'} \iint\limits_{\Omega^e_{00}\cap\Omega^u_{-m'-n'}} \boldsymbol{J}^e_{00}(\boldsymbol{r}') e^{j\boldsymbol{\rho}'\cdot\boldsymbol{k}^{pq}_\rho} e^{j(m'\boldsymbol{S}_a + n'\boldsymbol{S}_b)\cdot(p\widetilde{\boldsymbol{S}}_a + q\widetilde{\boldsymbol{S}}_b)} d\boldsymbol{\rho}' \end{aligned} \tag{45}$$

Substitute (34) into (45), we have

$$\widetilde{\boldsymbol{J}}^u\left(\boldsymbol{k}^{pq}_\rho, z\right) = \sum_{m'} \sum_{n'} \iint\limits_{\Omega^e_{00}\cap\Omega^u_{-m'-n'}} \boldsymbol{J}^e_{00}(\boldsymbol{r}') e^{j\boldsymbol{\rho}'\cdot\boldsymbol{k}^{pq}_\rho} d\boldsymbol{\rho}'$$

$$= \iint\limits_{\Omega_{00}^e} \boldsymbol{J}_{00}^e(\boldsymbol{r}') e^{j\boldsymbol{\rho}'\cdot\boldsymbol{k}_\rho^{pq}} d\boldsymbol{\rho}'$$
$$= \iint\limits_{\Omega_{00}^e} \boldsymbol{J}^e(\boldsymbol{r}') e^{j\boldsymbol{\rho}'\cdot\boldsymbol{k}_\rho^{pq}} d\boldsymbol{\rho}' = \widetilde{\boldsymbol{J}}^e\left(\boldsymbol{k}_\rho^{pq}, z\right), \tag{46}$$

Although the spatial-domain element current and unit cell current are quite different, their spectrums are identical, as described in (46).

3.1.5. Scattered Field from an Freestanding FSS in Terms of Spectral-domain Element Current

From the relationship between the spectral-domain unit cell current and the spectral-domain element current as specified in (46), we have

$$\widetilde{\boldsymbol{E}}^{sa}(z) = \left[\overline{\overline{\widetilde{\boldsymbol{G}}}}_h\left(\boldsymbol{k}_\rho^{pq}, z, z'\right) \cdot \widetilde{\boldsymbol{J}}_l^e\left(\boldsymbol{k}_\rho^{pq}, z'\right)\right]_{z'=0}, \tag{47}$$

Obviously, it is more convenient to use (47) because it is more natural to define spatial-domain current over an actual array element.

3.1.6. Scattered Field from Multiple FSS Screens Embedded in Multilayered Dielectric Structure

As shown in Fig. 1, a practical FSS structure may contain more than one array. In addition, the arrays are usually supported by substrates and/or covered by superstrates. In this case, (38) still holds. However,

$$\widetilde{\boldsymbol{E}}^{sa}\left(\boldsymbol{k}_\rho^{pq}, z\right) = \sum_{l=1}^{L} \overline{\overline{\widetilde{\boldsymbol{G}}}}\left(\boldsymbol{k}_\rho^{pq}, z, z_{I_l}\right) \cdot \widetilde{\boldsymbol{J}}_l^u\left(\boldsymbol{k}_\rho^{pq}, z_{I_l}\right)$$
$$= \sum_{l=1}^{L} \overline{\overline{\widetilde{\boldsymbol{G}}}}\left(\boldsymbol{k}_\rho^{pq}, z, z_{I_l}\right) \cdot \widetilde{\boldsymbol{J}}_l^e\left(\boldsymbol{k}_\rho^{pq}, z_{I_l}\right), \tag{48}$$

where I_l is the index of the interface on which the lth array lies.

3.2. Galerkin's Implementation

Expand the element current as

$$\boldsymbol{J}_l^e(\boldsymbol{r}) = \sum_{i=1}^{M} I_{li}^e \boldsymbol{B}_{li}^e(\boldsymbol{r}) \quad \boldsymbol{r} \in \Omega_{00l}^e, \tag{49}$$

where Ω^e_{00l} is the domain of the reference element domain of array l, $\boldsymbol{B}^e_{li}(\boldsymbol{r})$ is the spatial-domain element current basis function which is non-zero over support Ω_{li}, I^e_{li} is the corresponding unknown expansion coefficient.

Implementing Galerkin's method over (38) with the boundary condition that the tangential electric field on the surface of conducting scatterers vanishes, we obtain the following matrix equation

$$\boldsymbol{V} = \boldsymbol{Z} \cdot \boldsymbol{I}, \tag{50}$$

where

$$\begin{aligned}
V_{li} &= -\int\limits_{\Omega_{li}} \boldsymbol{B}^e_{li}(\boldsymbol{r}) \left[\hat{n} \times \boldsymbol{E}^{ex}_l(\boldsymbol{r})\right] d\boldsymbol{\rho} \\
&= -\widetilde{\boldsymbol{B}}^e_{li}\left(-\boldsymbol{k}^{inc}_\rho, z_{I_l}\right) \cdot \left[\hat{n} \times \widetilde{\boldsymbol{E}}^{ex}_l\left(\boldsymbol{k}^{inc}_\rho, z_{I_l}\right)\right] \\
Z_{l_1 i l_2 j} &= \frac{1}{T_a T_b} \int\limits_{\Omega_{l_1 i}} \boldsymbol{B}^e_{l_1 i}(\boldsymbol{r}) \left[\hat{n} \times \sum_{p=-\infty}^{\infty} \sum_{q=-\infty}^{\infty} \overline{\overline{\widetilde{\boldsymbol{G}}}}\left(\boldsymbol{k}^{pq}_\rho, z_{I_{l_1}}, z_{I_{l_2}}\right)\right. \\
&\qquad \left. \cdot \widetilde{\boldsymbol{B}}^e_{l_2 j}\left(\boldsymbol{k}^{pq}_\rho, z_{I_{l_2}}\right) e^{-j\boldsymbol{\rho}\cdot\boldsymbol{k}^{pq}_\rho}\right] d\boldsymbol{\rho} \\
&= \frac{1}{T_a T_b} \left[\sum_{p=-\infty}^{\infty} \sum_{q=-\infty}^{\infty} \widetilde{\boldsymbol{B}}^e_{l_1 j}\left(-\boldsymbol{k}^{pq}_\rho, z_{I_{l_1}}\right) \cdot \hat{n}\right. \\
&\qquad \left. \times \overline{\overline{\widetilde{\boldsymbol{G}}}}\left(\boldsymbol{k}^{pq}_\rho, z_{I_{l_1}}, z_{I_{l_2}}\right) \cdot \widetilde{\boldsymbol{B}}^e_{l_2 j}\left(\boldsymbol{k}^{pq}_\rho, z_{I_{l_2}}\right)\right],
\end{aligned} \tag{51}$$

where $\boldsymbol{E}^{ex}_l(\boldsymbol{r})$ and $\widetilde{\boldsymbol{E}}^{ex}_l(\boldsymbol{k}^{inc}_\rho, z_{I_l})$ are the spatial- and spectral-domain excitation fields at interface I_l, $\boldsymbol{E}^{ex}_l(\boldsymbol{r}) = \widetilde{\boldsymbol{E}}^{ex}_l(\boldsymbol{k}^{inc}_\rho, z) e^{-j\boldsymbol{k}^{inc}_\rho \cdot \boldsymbol{\rho}}$, $\widetilde{\boldsymbol{B}}^e_{li}(\boldsymbol{k}^{inc}_\rho, z)$ is the spectral-domain current basis function.

$\boldsymbol{E}^{ex}_l(\boldsymbol{r})$ is the total electric field from the multilayered dielectric structure without any FSS screens embedded when the multilayered dielectric structure is illuminated by plane wave specified in (4). It can also be decomposed into components parallel and perpendicular to the plane of incidence. Its expression can be found in textbooks on stratified media such as [22].

Noting that neither $\widetilde{\boldsymbol{B}}^e_{l_1 i}(\boldsymbol{k}^{pq}_\rho, z_{I_l})$ nor $\widetilde{\boldsymbol{B}}^e_{l_2 i}(\boldsymbol{k}^{pq}_\rho, z_{I_l})$ has z-component for the concerned array elements, (51) can be rewritten as

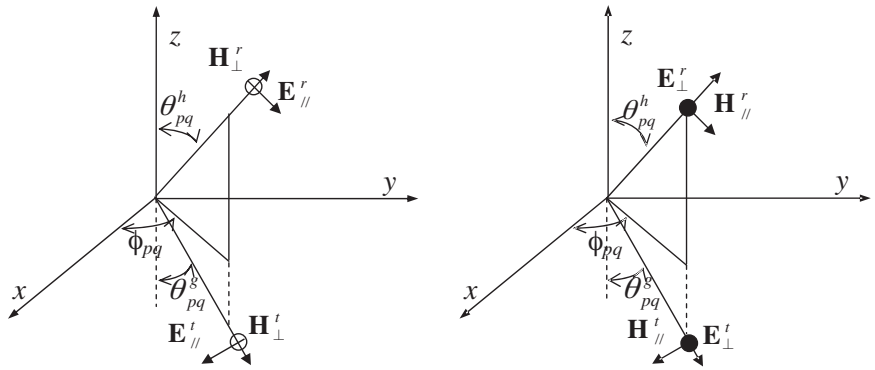

Figure 5. Plane of reflection and transmission and polarization of reflected and transmitted fields (left: parallel polarization, right: perpendicular polarization).

$$Z_{l_1 i l_2 j} = \frac{1}{T_a T_b} \widetilde{\boldsymbol{B}}_{l_1 i}^{e}\left(-\boldsymbol{k}_{\rho}^{pq}, z_{I_{l_1}}\right) \times \left[\hat{n} \times \sum_{p=-\infty}^{\infty} \sum_{q=-\infty}^{\infty} \widetilde{\overline{\overline{\boldsymbol{G}}}}^{\rho}\left(\boldsymbol{k}_{\rho}^{pq}, z_{I_{l_1}}, z_{I_{l_2}}\right) \cdot \widetilde{\boldsymbol{B}}_{l_2 j}^{e}\left(\boldsymbol{k}_{\rho}^{pq}, z_{I_{l_2}}\right)\right], \quad (52)$$

where [5, 23]

$$\widetilde{\overline{\overline{\boldsymbol{G}}}}^{\rho}(\boldsymbol{k}_{\rho}, z_i, z_j) = -\begin{bmatrix} Z^{h,ij}\sin^2\phi + Z^{e,ij}\cos^2\phi & (Z^{e,ij} - Z^{h,ij})\cos\phi\sin\phi \\ (Z^{e,ij} - Z^{h,ij})\cos\phi\sin\phi & Z^{e,ij}\sin^2\phi + Z^{h,ij}\cos^2\phi \end{bmatrix}, \quad (53)$$

the superscript e corresponds to the TM case, and the superscript h corresponds to the TE case,

$$\cos\phi = \alpha/\sqrt{\alpha^2+\beta^2}$$
$$\sin\phi = \beta/\sqrt{\alpha^2+\beta^2}$$

In particular, for normal incidence and mode 00, $\alpha = \beta = 0,\ \phi = \phi^{inc}$.

The formulation of $Z^{e/h,ij} = Z^{e/h}(z_i, z_j)$ in (53) has been given in [5, 18].

Please note the sign error in [5, 6] and [23] with respect to $\widetilde{\overline{\overline{\boldsymbol{G}}}}^{\rho}(\boldsymbol{k}_{\rho}, z_i, z_j)$. Please also note that we are using symbol ϕ instead of θ as used in [1, 5, 6] and [23]. In fact, θ there is confusing.

3.3. Reflection and Transmission Coefficients

3.3.1. Plane of Reflection and Transmission of Mode (p, q)

The reflection and transmission coefficients are defined with respect to the plane of reflection and transmission of mode (p, q). The plane of reflection of mode (p, q) is defined by the reflection propagation vector $\boldsymbol{k}_{pq}^{r}$ and the interface normal $\hat{n} = \hat{z}$, as shown in Fig. 5. The plane of transmission of mode (p, q) is similarly defined. In fact, the plane of reflection of mode (p, q) is also the plane of transmission of mode (p, q).

3.3.2. Reflection and Transmission Coefficients of Mode (p, q)

The total spectral-domain reflected and transmitted fields of mode (p, q) from the FSS structure are

$$\begin{aligned}\widetilde{\boldsymbol{E}}^{r}\left(\boldsymbol{k}_{\rho}^{pq}, z\right) &= \delta_{p0}\delta_{q0}\widetilde{\boldsymbol{E}}_{0}^{r}\left(\boldsymbol{k}_{\rho}^{inc}, z\right) + \widetilde{\boldsymbol{E}}^{sa}\left(\boldsymbol{k}_{\rho}^{pq}, z\right) \\ &= \widetilde{\boldsymbol{E}}^{r}\left(\boldsymbol{k}_{\rho}^{pq}, z_0\right) e^{-jk_{zpq}^{h}(z-z_0)}, \qquad (54)\\ \widetilde{\boldsymbol{E}}^{t}\left(\boldsymbol{k}_{\rho}^{pq}, z\right) &= \delta_{p0}\delta_{q0}\widetilde{\boldsymbol{E}}_{0}^{t}\left(\boldsymbol{k}_{\rho}^{inc}, z\right) + \widetilde{\boldsymbol{E}}^{sa}\left(\boldsymbol{k}_{\rho}^{pq}, z\right) \\ &= \widetilde{\boldsymbol{E}}^{t}\left(\boldsymbol{k}_{\rho}^{pq}, z_N\right) e^{jk_{zpq}^{g}(z-z_N)}, \qquad (55)\end{aligned}$$

where

$$\widetilde{\boldsymbol{E}}_{0}^{r/t}\left(\boldsymbol{k}_{\rho}^{inc}, z\right) = \begin{cases} \widetilde{\boldsymbol{E}}_{0\parallel}^{r/t}\left(\boldsymbol{k}_{\rho}^{inc}, z\right) & \text{parallel incidence} \\ \widetilde{\boldsymbol{E}}_{0\perp}^{r/t}\left(\boldsymbol{k}_{\rho}^{inc}, z\right) & \text{perpendicular incidence} \end{cases}$$

$\widetilde{\boldsymbol{E}}_{0\parallel}^{r/t}\left(\boldsymbol{k}_{\rho}^{inc}, z\right)$ and $\widetilde{\boldsymbol{E}}_{0\perp}^{r/t}\left(\boldsymbol{k}_{\rho}^{inc}, z\right)$ are the reflected/transmitted field of parallel or perpendicular polarization when the multilayered dielectric structure without planar periodic screens embedded is illuminated by incident plane wave of parallel or perpendicular polarization.

$\widetilde{\boldsymbol{E}}^{r}(\boldsymbol{k}_{\rho}^{pq}, z_0)$ is decomposed into parallel $(\hat{\theta}_{pq}^{r} = \hat{\theta}_{pq}^{h})$ and perpendicular $(-\hat{\phi}_{pq})$ components with respect to the plane of reflection of mode (p, q)

$$\widetilde{\boldsymbol{E}}^{r}\left(\boldsymbol{k}_{\rho}^{pq}, z_0\right) = \left(\widetilde{\boldsymbol{E}}_{pq}^{r}\right)_{\parallel} + \left(\widetilde{\boldsymbol{E}}_{pq}^{r}\right)_{\perp}, \qquad (56)$$

where

$$\left(\widetilde{\boldsymbol{E}}_{pq}^{r}\right)_{\parallel} = \hat{\theta}_{pq}^{r} R_{pi}^{\parallel} \qquad \left(\widetilde{\boldsymbol{E}}_{pq}^{r}\right)_{\perp} = -\hat{\phi}_{pq} R_{pi}^{\perp}$$

the subscript pi stands for the polarization of incident plane wave.

Similarly, $\widetilde{\boldsymbol{E}}^t(\boldsymbol{k}_\rho^{pq}, z_N)$ is decomposed into components parallel ($\hat{\theta}_{pq}^t = \hat{\theta}_{pq}^g$) and perpendicular ($-\hat{\phi}_{pq}$) to the plane of transmission of mode (p,q) which is also the plane of reflection of mode (p,q)

$$\widetilde{\boldsymbol{E}}^t\left(\boldsymbol{k}_\rho^{pq}, z_N\right) = \left(\widetilde{\boldsymbol{E}}_{pq}^t\right)_\parallel + \left(\widetilde{\boldsymbol{E}}_{pq}^t\right)_\perp, \tag{57}$$

where

$$\left(\widetilde{\boldsymbol{E}}_{pq}^t\right)_\parallel = \hat{\theta}_{pq}^t T_{pi}^\parallel \qquad \left(\widetilde{\boldsymbol{E}}_{pq}^t\right)_\perp = -\hat{\phi}_{pq} T_{pi}^\perp, \tag{58}$$

Therefore, the reflection and transmission coefficients are defined as

$$R_{pi}^{pr} = \left(\widetilde{\boldsymbol{E}}_{pq}^r\right)_{pr} \cdot \hat{p}_{pq}^{pr} / \boldsymbol{E}_{0pi}^{inc} \cdot \hat{p}_{pi}^{inc}, \tag{59}$$

$$T_{pi}^{pt} = \left(\widetilde{\boldsymbol{E}}_{pq}^t\right)_{pt} \cdot \hat{p}_{pq}^{pt} / \boldsymbol{E}_{0pi}^{inc} \cdot \hat{p}_{pi}^{inc}, \tag{60}$$

where the superscripts/subscripts pr and pt are the polarization (parallel, $\parallel$, or perpendicular, $\perp$) of reflected and transmitted fields respectively, $\hat{p}_{pq}^{pr}$, $\hat{p}_{pq}^{pt}$ and $\hat{p}_{pi}^{inc}$ are the corresponding unit polarization vectors of reflected, transmitted and incident fields.

Although the definition in (59) and (60) is very clear, it is computationally inefficient since $(\widetilde{\boldsymbol{E}}_{pq}^r)_{pr}$ and $(\widetilde{\boldsymbol{E}}_{pq}^t)_{pt}$ may have z-component. Alternatively, the reflection and transmission coefficients can be computed using the azimuthal components of the reflected and transmitted fields only.

It is straightforward to compute $R_{pi}^\perp$ and $T_{pi}^\perp$ since $\hat{\phi}_{pq}$ is orthogonal to $\hat{\theta}_{pq}^r$, $\hat{\theta}_{pq}^t$ and $\hat{z}$,

$$R_{pi}^\perp = -\widetilde{\boldsymbol{E}}^r\left(\boldsymbol{k}_\rho^{pq}, z_0\right) \cdot \hat{\phi}_{pq}, \tag{61}$$

$$T_{pi}^\perp = -\widetilde{\boldsymbol{E}}^t\left(\boldsymbol{k}_\rho^{pq}, z_N\right) \cdot \hat{\phi}_{pq}, \tag{62}$$

We are then able to compute $R_{pi}^\parallel$ and $T_{pi}^\parallel$ as

$$R_{pi}^\parallel = -\frac{\left(\widetilde{\boldsymbol{E}}_{pq}^r\right)_\parallel \cdot \widetilde{\hat{\rho}}_{pq}}{k_{zpq}^h / k_h} = -\frac{\left(\widetilde{\boldsymbol{E}}_{pq}^r\right)_\parallel^\rho \cdot \widetilde{\hat{\rho}}_{pq}}{k_{zpq}^h / k_h}, \tag{63}$$

$$T_{pi}^\parallel = \frac{\left(\widetilde{\boldsymbol{E}}_{pq}^t\right)_\parallel \cdot \widetilde{\hat{\rho}}_{pq}}{k_{zpq}^g / k_g} = \frac{\left(\widetilde{\boldsymbol{E}}_{pq}^t\right)_\parallel^\rho \cdot \widetilde{\hat{\rho}}_{pq}}{k_{zpq}^g / k_g}, \tag{64}$$

where $(\widetilde{\boldsymbol{E}}_{mn}^r)_\parallel^\rho$ and $(\widetilde{\boldsymbol{E}}_{mn}^t)_\parallel^\rho$ are the azimuthal components of $(\widetilde{\boldsymbol{E}}_{pq}^r)_\parallel$ and $(\widetilde{\boldsymbol{E}}_{pq}^t)_\parallel$.

4. NUMERICAL RESULTS

4.1. Introduction

In this section, we will validate the VSM by applying it to analyze some typical FSS structures and comparing the simulation results with published and experimental results.

Experimental data come from two sources. Most of the measurement is carried out by Dr. K. M. Hock. Incident elevation angles vary between 0° and 60° while incident azimuthal angles may take 0°, ψ, 90°, and $\psi + 90°$. The transmission coefficients of the FSS structure with double-square array is provided by Prof. C. K. Lee and manually reproduced from his Ph.D. dissertation [24] by this author.

Thin array elements are studied. Although the VSM imposes no restriction on array elements, simulation of FSS structures with thin array elements is computationally much cheaper.

Piecewise sinusoidal basis and testing functions are used. Monopole is shorter than 0.1 wavelength of the residing material. Thin wire approximation is applied to reduce the computational complexity.

4.2. FSS Structures with Single Array

4.2.1. FSS Structure with y-directed Thin Dipole Array

The first FSS structure is shown in Fig. 6. It is an FSS structure with y-directed thin dipole array. The reflection and transmission coefficients at normal incidence ($\theta^{inc} = 0°, \phi^{inc} = 90°$) are shown in Fig. 6 where the experimental results are also given. Agreement is very good.

4.2.2. FSS Structure with 45°-directed Thin Dipole Array

Next, consider a 45°-directed thin dipole array as shown in Fig. 7(a). Here, we consider two sets of incident angles, ($\theta^{inc} = 0°, \phi^{inc} = 45°$) and ($\theta^{inc} = 0°, \phi^{inc} = 0°$). The corresponding reflection and transmission coefficients are shown in Figs. 7(b) and 7(c). Apparently, simulation results agree very well with experimental results.

4.2.3. FSS Structure with Staggered y-directed Thin Dipole Array

The third FSS structure considered is one with staggered y-directed thin dipole array as shown in Fig. 8. Again, normal incidence ($\theta^{inc} = 0°, \phi^{inc} = 90°$) is simulated. The simulation results and experimental results are shown in Figs. 8(b) and 8(c). The agreement is fairly good.

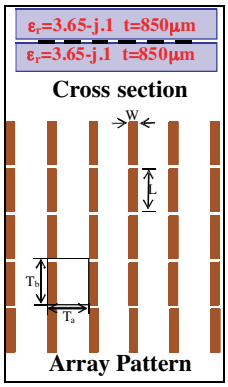

Figure 6. An FSS structure with y-directed thin dipole array ($T_a = 9\,\text{mm}$, $T_b = 9\,\text{mm}$, $L = 8\,\text{mm}$, $W = 80\,\mu\text{m}$, metal thickness: $17.5\,\mu\text{m}$, $\theta^{inc} = 0°, \phi^{inc} = 90°$).

4.2.4. FSS Structure with Type-2 Gangbuster Array

Here, we study two examples. The first example studied is shown in Fig. 9(a). Three cases of normal incidence, ($\theta^{inc} = 0°, \phi^{inc} = \tan^{-1} 2$), ($\theta^{inc} = 0°, \phi^{inc} = 0°$), and ($\theta^{inc} = 0°, \phi^{inc} = 90°$), are simulated. In general, the simulation results agree well with experimental results.

We have also simulated the FSS structure shown in Fig. 10. Oblique incidence is considered. The simulation results agree perfectly with those given in [4].

4.2.5. FSS Structure with Double-Square Array

The last structure in this category studied is an FSS structure with double-square array as shown in Fig. 11(a). Both normal and oblique incidences are considered. In general, good agreement is observed. However, it must be pointed out here that the agreement at higher frequencies is worse since the thin wire approximation becomes less and less valid as frequency goes higher and higher.

4.3. FSS Structures with Multiple Arrays

The previous FSS structures contain one array only. Sometimes, more than one array are applied in one FSS structure. Here, VSM is applied to analyze FSS structures with multiple arrays. Two structures are studied.

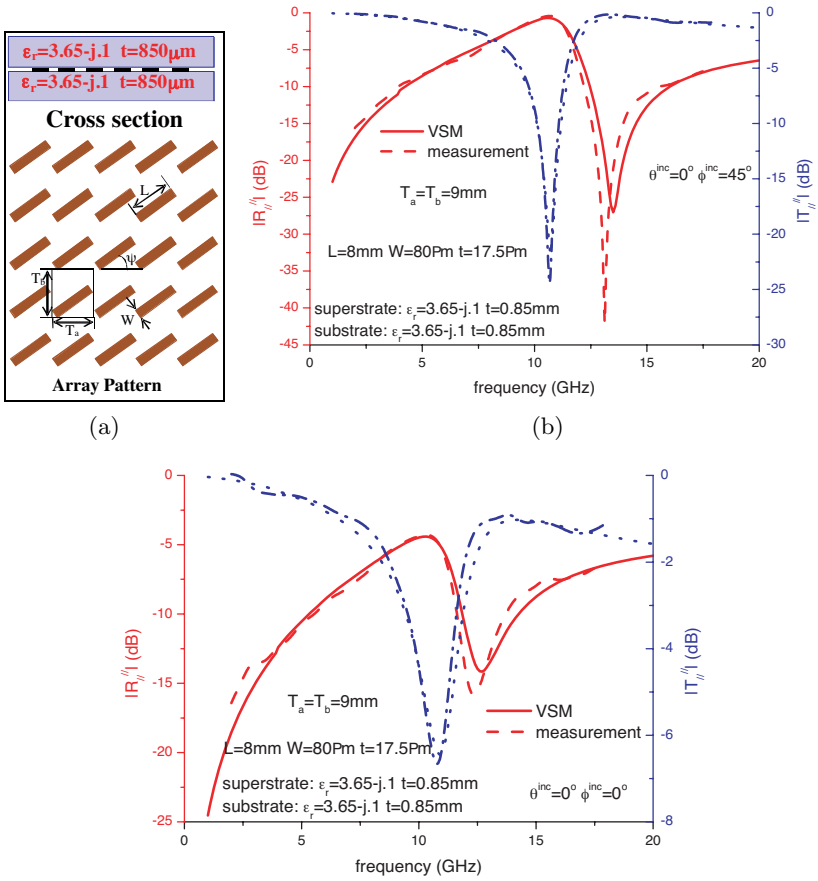

Figure 7. An FSS structure with 45°-directed thin dipole array (a) Configuration ($T_a = 9\,\text{mm}$, $T_b = 9\,\text{mm}$, $L = 8\,\text{mm}$, $W = 80\,\mu\text{m}$, $\psi = 45°$, metal thickness: $17.5\,\mu\text{m}$) (b) Reflection coefficients and transmission coefficients ($\theta^{inc} = 0°, \phi^{inc} = 45°$) (c) Reflection and transmission coefficients ($\theta^{inc} = 0°, \phi^{inc} = 0°$).

4.3.1. FSS Structure with Two Thin Dipole Arrays

The first structure contains two thin dipole arrays. The structure consists of the FSS structures shown in Figs. 6 and 8. The two structures are separated by a spacer. The side view of this structure is shown in Fig. 12(a).

Two cases are considered. For the first case, the y-directed thin

dipole array acts as array #1 while the staggered y-directed thin dipole array acts as array #2. Incidences ($\theta^{inc} = 0°, \phi^{inc} = 90°$) and ($\theta^{inc} = 10°, \phi^{inc} = 90°$) are studied. The reflection and transmission coefficients are given in Figs. 12(b) and 12(c). Agreement is good.

For the second case, the two arrays are reversed, i.e., the y-directed thin dipole array serves as array #2 while the staggered y-directed thin dipole array serves as array #1. The reflection and transmission coefficients for ($\theta^{inc} = 0°, \phi^{inc} = 90°$) is given in Fig. 12(d). Similar agreement is observed.

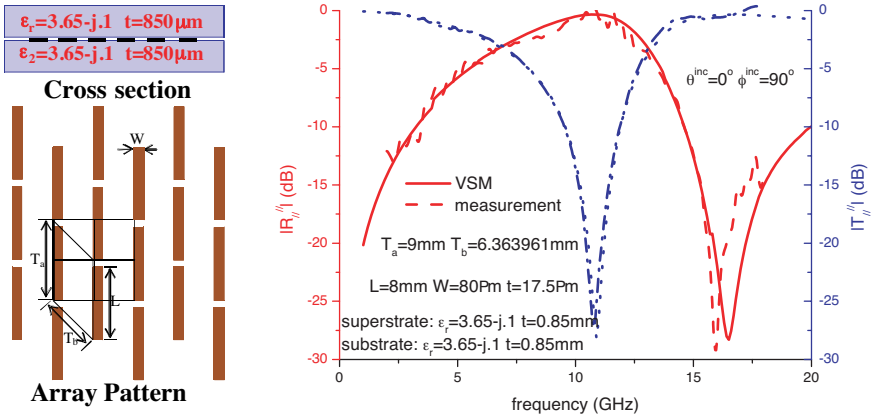

Figure 8. An FSS structure with staggered y-directed thin dipole array ($T_a = 9\,\text{mm}$, $T_b = 4.5\,\text{mm}$, $L = 8\,\text{mm}$, $W = 80\,\mu\text{m}$, metal thickness: $17.5\,\mu\text{m}$, $\theta^{inc} = 0°, \phi^{inc} = 90°$).

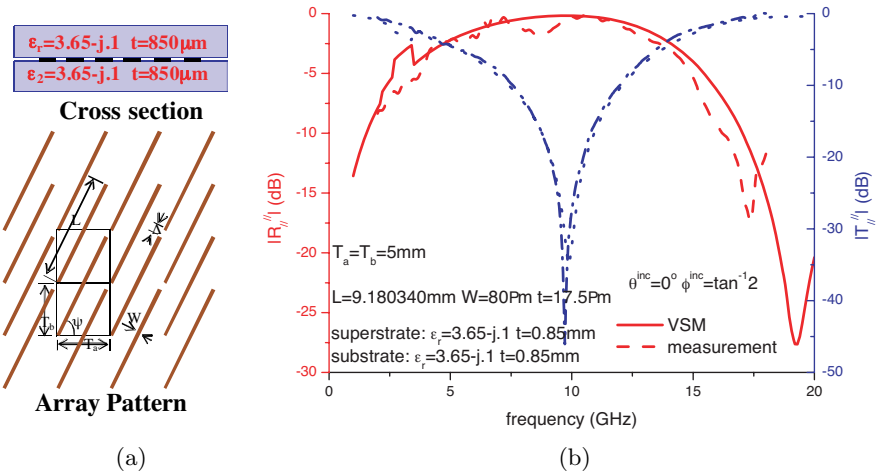

(a) (b)

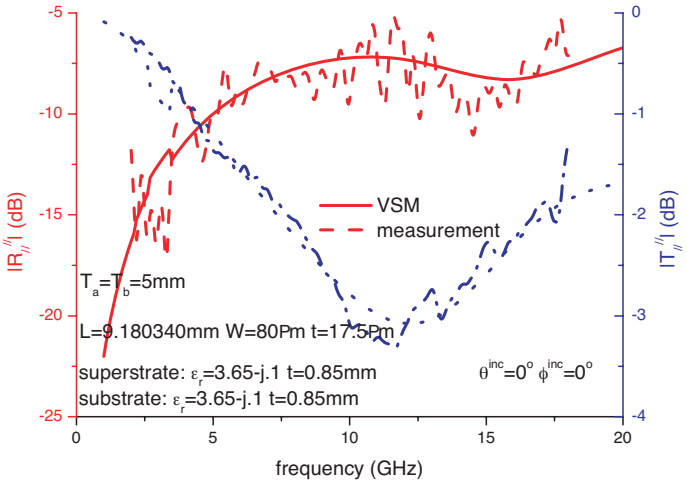

(c)

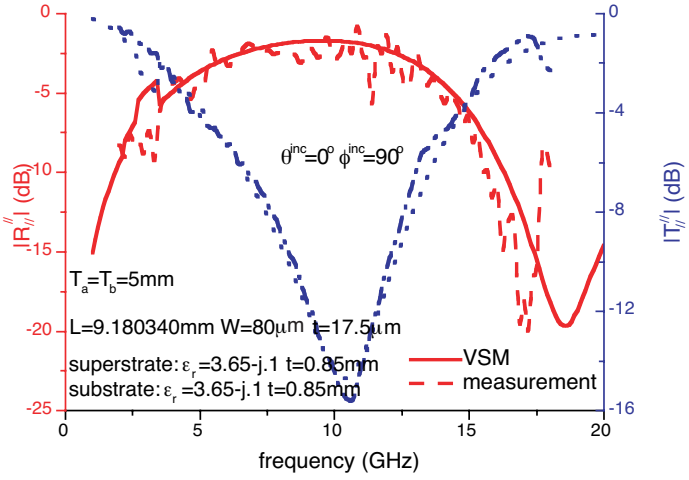

(d)

Figure 9. An FSS structure with Type-2 gangbuster array (a) Configuration ($T_a = 5\,\text{mm}$, $T_b = 5\,\text{mm}$, $L = \sqrt{T_a^2 + (2T_b)^2} - \Delta$, $\Delta = 2\,\text{mm}$, $W = 80\,\mu\text{m}$, $\psi = \tan^{-12}$) (b) Reflection and transmission coefficient ($\theta^{inc} = 0°, \phi^{inc} = \tan^{-1}2$) (c) Reflection coefficients and transmission coefficients ($\theta^{inc} = 0°, \phi^{inc} = 0°$) (d) Reflection and transmission coefficient ($\theta^{inc} = 0°, \phi^{inc} = 90°$).

It is noticed that the periodicity of the two arrays in this structure is different. Therefore, this example also serves to demonstrate that VSM is able to deal with FSS structures with multiple arrays whose periodicity satisfies (2).

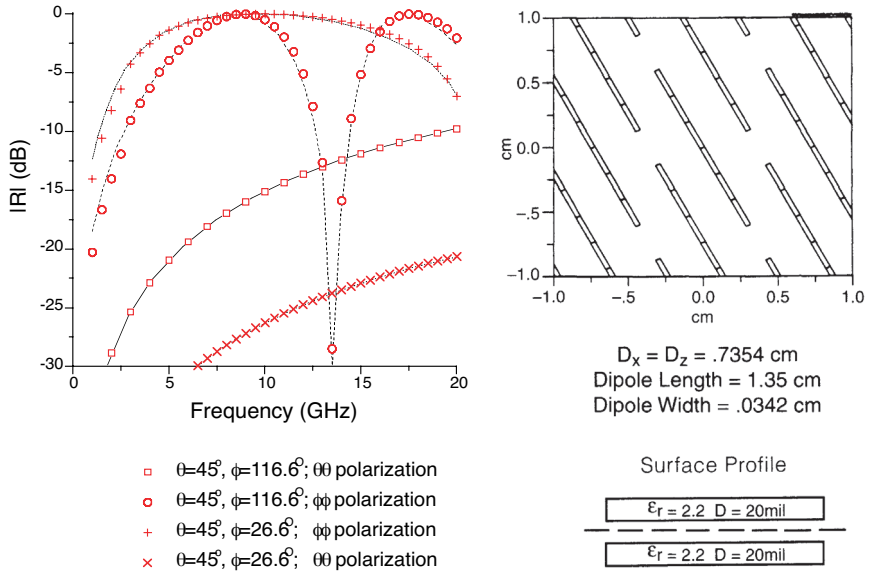

Figure 10. An FSS Sstructure with Type-2 gangbuster array studied in [4].

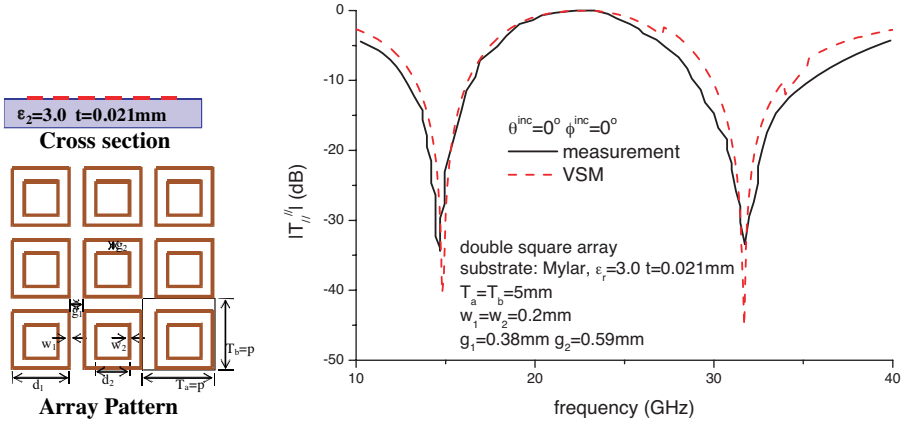

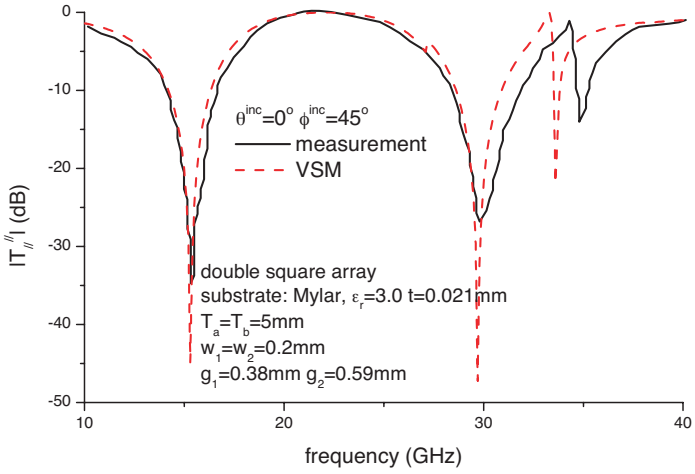

(c)

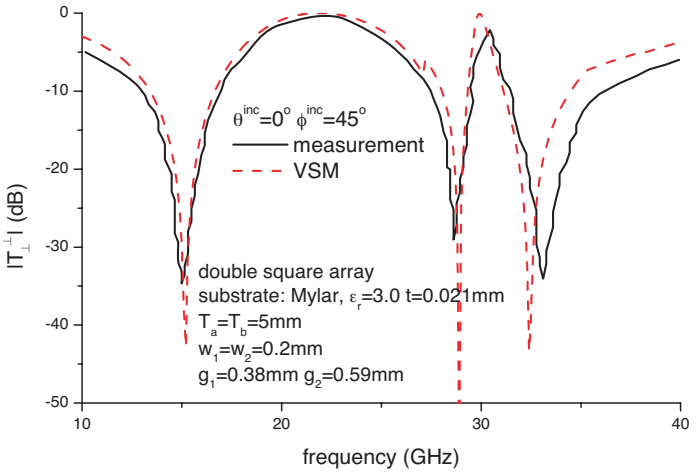

(d)

Figure 11. An FSS structure with double-square array (a) Configuration ($T_a = T_b = 5\,\text{mm}$, $d_1 = 4.62\,\text{mm}$, $d_2 = 3.04\,\text{mm}$, $w_1 = w_2 = 0.2\,\text{mm}$, $g_1 = 0.38\,\text{mm}$, $g_2 = 0.59\,\text{mm}$, metal thickness: 21 (m) (b) Transmission coefficient ($\theta^{inc} = 0°, \phi^{inc} = 0°$) (c) Transmission coefficient ($\theta^{inc} = 45°, \phi^{inc} = 0°$) (d) Transmission coefficient ($\theta^{inc} = 45°, \phi^{inc} = 0°$).

4.3.2. FSS Structure with Four Thin Dipole Arrays

The final structure investigated contains four thin dipole arrays. The structure is formed by assemble the structures studied in Subsections 4.2.1 and 4.2.2 in the way shown in Fig. 13(a). For symmetry, the thickness of spacers 1 and 3 are identical. Three cases of spacer thickness are studied. The corresponding reflection and transmission coefficients are given in Figs. 13(b)–13(g). The agreement between simulation results and experimental results is satisfactory.

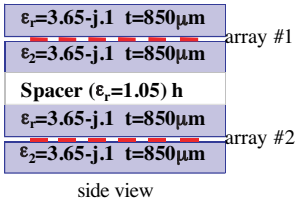

(a)

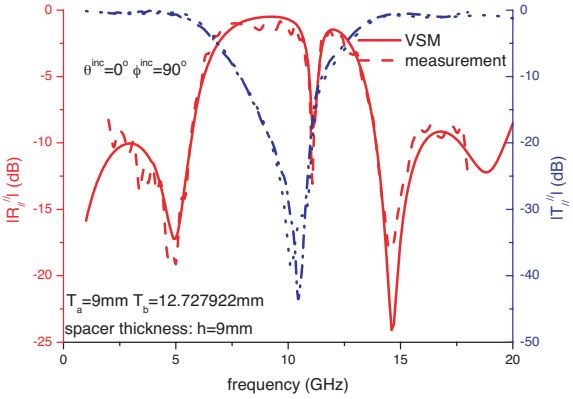

(b)

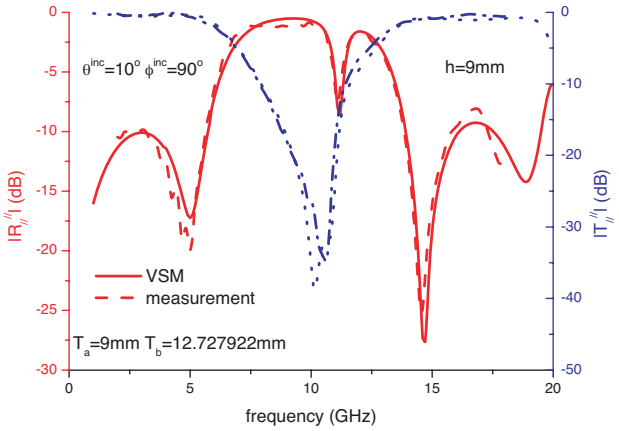

(c)

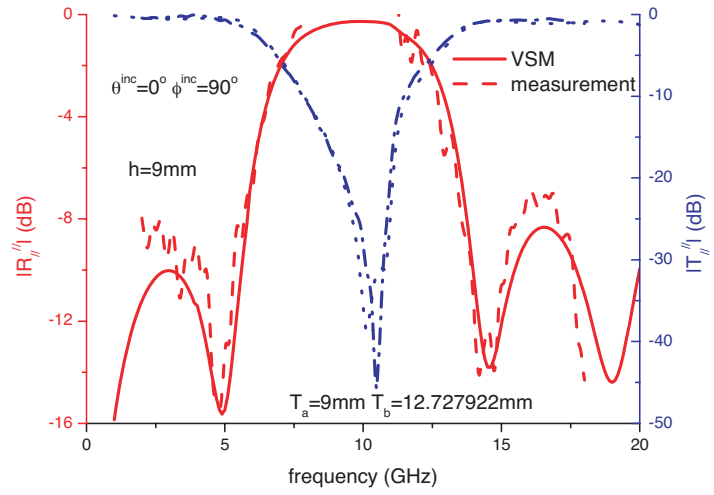

(d)

Figure 12. An FSS structure with two thin dipole arrays (a) Configuration (b) Reflection and transmission coefficients (array #1: y-directed thin dipole array in Fig. 5, array #2: staggered y-directed thin dipole array in Fig. 7, $\theta^{inc} = 0°, \phi^{inc} = 90°$) (c) Reflection and transmission coefficients (array #1: y-directed thin dipole array in Fig. 5, array #2: staggered y-directed thin dipole array in Fig. 7, $\theta^{inc} = 10°, \phi^{inc} = 90°$) (d) Reflection and transmission coefficients (array #1: staggered y-directed thin dipole array in Fig. 7, array #2: y-directed thin dipole array in Fig. 5, $\theta^{inc} = 0°, \phi^{inc} = 90°$).

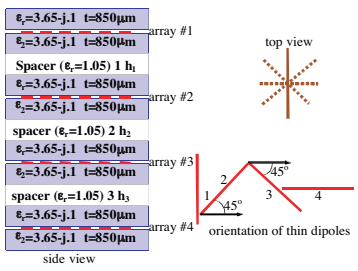

(a)

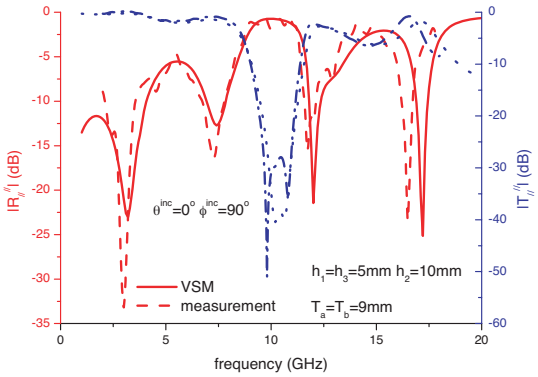

(b)

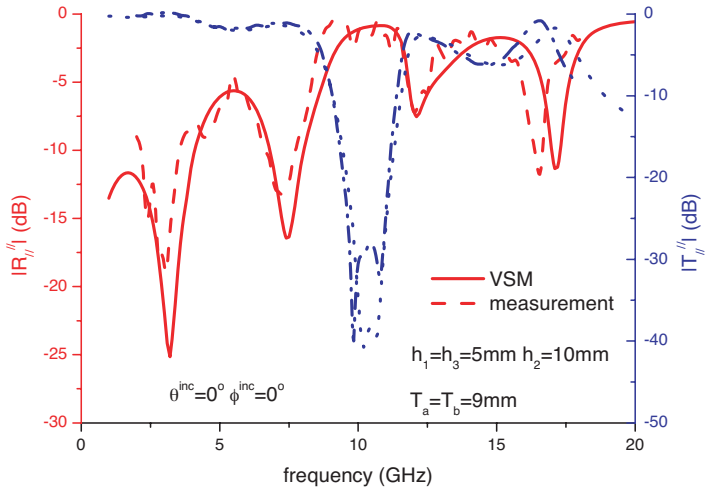
VSM
measurement
h1=h3=5mm h2=10mm
Ta=Tb=9mm
θinc=0° φinc=0°
frequency (GHz)
|R//| (dB)
|T//| (dB)

(c)

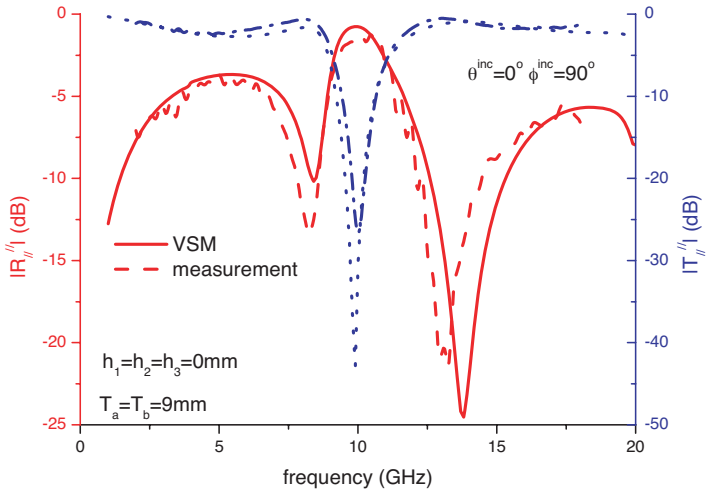
VSM
measurement
h1=h2=h3=0mm
Ta=Tb=9mm
θinc=0° φinc=90°
frequency (GHz)
|R//| (dB)
|T//| (dB)

(d)

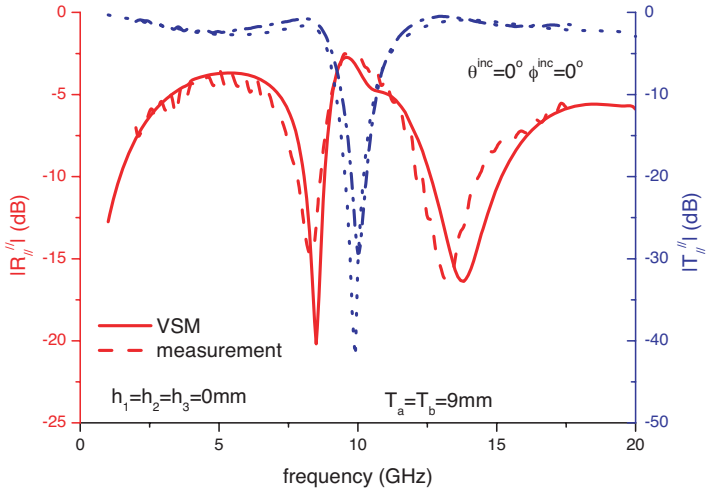
θ^inc=0° φ^inc=0°
VSM
measurement
h1=h2=h3=0mm
Ta=Tb=9mm
frequency (GHz)
|R//| (dB)
|T//| (dB)

(e)

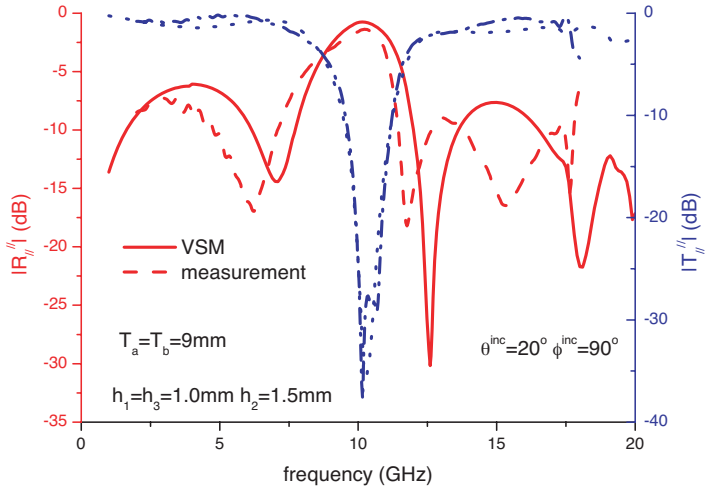
VSM
measurement
Ta=Tb=9mm
h1=h3=1.0mm h2=1.5mm
θ^inc=20° φ^inc=90°
frequency (GHz)
|R//| (dB)
|T//| (dB)

(f)

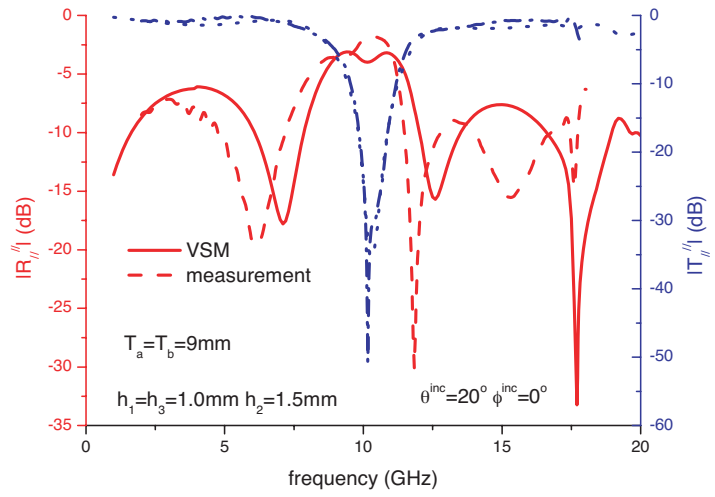

(g)

Figure 13. An FSS structure with four thin dipole arrays (a) Configuration (b) Reflection and transmission coefficient ($\theta^{inc} = 0°, \phi^{inc} = 90°$, $h_1 = h_3 = 5\,\text{mm}$, $h_2 = 10\,\text{mm}$) (c) Reflection coefficient and transmission coefficient ($\theta^{inc} = 0°, \phi^{inc} = 0°$, $h_1 = h_3 = 5\,\text{mm}$, $h_2 = 10\,\text{mm}$) (d) Reflection and transmission coefficient ($\theta^{inc} = 0°, \phi^{inc} = 90°$, $h_1 = h_2 = h_3 = 0$) (e) Reflection and transmission coefficient ($\theta^{inc} = 0°, \phi^{inc} = 0°$, $h_1 = h_2 = h_3 = 0$) (f) Reflection and transmission coefficient ($\theta^{inc} = 20°, \phi^{inc} = 90°$, $h_1 = h_3 = 1.0\,\text{mm}$ $h_2 = 1.5\,\text{mm}$) (g) Reflection and transmission coefficient ($\theta^{inc} = 20°, \phi^{inc} = 0°$, $h_1 = h_3 = 1.0\,\text{mm}$ $h_2 = 1.5\,\text{mm}$).

5. CONCLUSIONS

Analysis of FSS structures is considered in this paper. VSM is developed following the basic idea of the standard SDM. It is shown that VSM is valid for spectral-domain surface current over both element domain and unit cell domain. The reflection and transmission coefficients based on vector electric and magnetic potentials are abandoned. Instead, electric field-based reflection and transmission coefficients are derived.

Extensive validation has been conducted by applying VSM to analyze various FSS structures. Excellent agreement is observed between simulation results and experimental results and published results.

ACKNOWLEDGMENT

The author would like to give special thanks to Dr. K. M. Hock and Prof. C. K. Lee for providing measurement results and Mr. X. Xu for helping this author to develop VSM. The authors also wish to thank Prof. C. H. Chan, Prof. R. Mittra, Dr. S. W. Yang, Dr. Y. Xu, Dr. M. Zhang, Mr. F. G. Hu, Dr. K. Y. Lum, Mr. Y. B. Gan, Dr. L. Liu and other colleagues for their fruitful discussions and constructive comments and suggestions.

The author would also like to give his sincere thanks to reviewers and editors for their constructive comments and suggestions to improve the quality of this paper.

REFERENCES

1. Mittra, R., C. H. Chan, and T. Cwik, "Techniques for analyzing frequency selective surfaces—a review," *IEEE Proc.*, Vol. 76, No. 12, 1593–1614, 1988.
2. Wu, T. K. (ed.), *Frequency Selective Surface and Grid Array*, Wiley, New York, 1995.
3. Vardaxoglou, J. C., *Frequency Selective Surfaces: Analysis and Design*, Wiley, New York, 1997.
4. Munk, B. A., *Frequency Selective Surfaces: Theory and Design*, Wiley, New York, 2000.
5. Chan, C. H., "Analysis of frequency selective surfaces," *Frequency Selective Surface and Grid Array*, T. K. Wu (ed.), Chap. 2, Wiley, New York, 1995.
6. Qing, A. and C. K. Lee, "An improved model for full wave analysis of multiplayered frequency selective surfaces with gridded square element," *Progress In Electromagnetics Research*, PIER 30, 285–303, 2001.
7. Langley, R. J. and E. A. Parker, "Equivalent circuit model for arrays of square loops," *Electron. Lett.*, Vol. 18, No. 7, 294–296, 1982.
8. Bardi, I., R. Remski, D. Perry, and Z. Cendes, "Plane wave scattering from frequency-selective surfaces by the finite-element method," *IEEE Trans. Magnetics*, Vol. 38, No. 2, 641–644, March 2002.
9. Harms, P., R. Mittra, and W. Ko, "Implementation of the periodic boundary condition in the finite-difference time-domain algorithm for FSS structures," *IEEE Trans. Antennas Propagat.*, Vol. 42, No. 9, 1317–1324, Sept. 1994.

10. Zheng, G., A. A. Kishk, A. W. Glisson, and A. B. Yakovlev, "Implementation of Mur's absorbing boundaries with periodic structures to speed up the design process using finite-difference time-domain method," *Progress In Electromagnetics Research*, PIER 58, 101–114, 2006.
11. Gurel, L. and W. C. Chew, "Recursive T-matrix algorithms for the solution of electromagnetic scattering from strip and patch geometries," *IEEE Trans. Antennas Propagat.*, Vol. 41, No. 1, 91–99, Jan. 1993.
12. Toyama, H. and K. Yasumoto, "Electromagnetic scattering from periodic arrays of composite circular cylinder with internal cylindrical scatterers," *Progress In Electromagnetics Research*, PIER 52, 321–333, 2005.
13. Ran, L., J. Huangfu, H. Chen, X. M. Zhang, K. Cheng, T. M. Grzegorczyk, and J. A. Kong, "Experimental study on several left-handed matamaterials," *Progress In Electromagnetics Research*, PIER 51, 249–279, 2005.
14. Chen, H., L. Ran, J. Huangfu, X. M. Zhang, K. Cheng, T. M. Grzegorczyk, and J. A. Kong, "Magnetic properties of S-shaped split-ring resonators," *Progress In Electromagnetics Research*, PIER 51, 231–247, 2005.
15. Lee, S. W., Y. Kuga, and A. Ishimaru, "Quasi-static analysis of materials with small tuneable stacked split sing resonators," *Progress In Electromagnetics Research*, PIER 51, 219–229, 2005.
16. Yao, H. Y., L. W. Li, Q. Wu, and J. A. Kong, "Macroscopic performance analysis of metamaterials synthesized from micrsocopic 2-D isotropic cross split-ring resonator array," *Progress In Electromagnetics Research*, PIER 51, 197–217, 2005.
17. Jorgenson, R. E., "Electromagnetic scattering from a structured slab comprised of periodically placed resistive cards," Ph.D. Dissertation, University of Illinois at Urbana-Champaign, 1989.
18. Tsao, C. H. and R. Mittra, "Spectral-domain analysis of frequency selective surfaces comprised of periodic arrays of cross dipoles and Jerusalem crosses," *IEEE Trans. Antennas Propagat.*, Vol. 32, No. 5, 478–486, May 1984.
19. Cwik, T. C. and R. Mittra, "Scattering from a periodic array of free-standing arbitrarily shaped perfectly conducting or resistive patches," *IEEE Trans. Antennas Propagat.*, Vol. 35, No. 11, 1226–1234, Nov. 1987.
20. Chan, C. H. and R. Mittra, "On the analysis of frequency-selective surfaces using subdomain basis functions," *IEEE Trans. Antennas. Propagat.*, Vol. 38, No. 1, 40–50, Jan. 1990.

21. Wakabayashi, H., M. Kominami, H. Kusaka, and H. Nakashima, "Numerical simulations for frequency-selective screens with complementary elements," *IEE Proc. Microw. Antennas Propagat.*, Vol. 141, No. 6, 477–482, Dec. 1994.
22. Kong, J. A., *Electromagnetic Wave Theory*, EMW Publishing, Cambridge, MA, 1999.
23. Itoh, T., "Spectral-domain immitance approach for dispersion characteristics of generalized printed transmission lines," *IEEE Trans. Microw. Theory Tech.*, Vol. 28, No. 7, 733–736, 1978.
24. Lee, C. K., "Modelling and design of frequency selective surfaces for reflector antennas," Ph.D. Dissertation, University of Kent at Canterbury, 1987.